Nanoscale

Accepted Manuscript

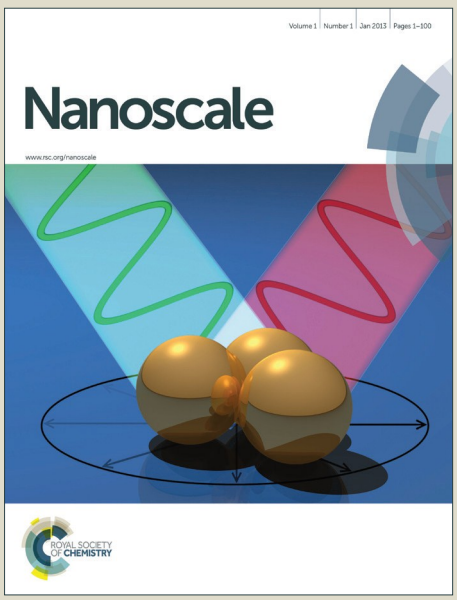

ROYAL SOCIETY OF CHEMISTRY

www.rsc.org/nanoscale

Nanodrop on a smooth solid surface with hidden roughness. Density functional theory considerations

Gersh O. Berim and Eli Ruckenstein*

Department of Chemical and Biological Engineering,

State University of New York at Buffalo,

Buffalo, New York 14260

March 17, 2015

*Author to whom correspondence should be addressed. Electronic mail: feaeliru@buffalo.edu; Phone number: (716)645-1179; Fax: (716)645-3822.

Abstract

A nanodrop of a test fluid placed on a smooth surface of a solid material of nonuniform density which covers a rough solid surface (hidden roughness) is examined, on the basis of the density functional theory (DFT), in the presence of an external perturbative force parallel to the surface. The contact angles which the drop profile makes with the surface at the leading edges of the drop are determined as functions of drop size and perturbative external force. A critical sticking force, defined as the largest value of the perturbative force for which the drop remains at equilibrium, is determined and its dependence on the size of the drop is explained on the basis of the shape of the interaction potential generated by the solid in vicinity of the leading edges of the drop. For even larger values of the perturbative force no drop-like solution of the Euler-Lagrange equation of the DFT was found. The upper bound of the inclination angle of a surface containing a macroscopic drop is estimated on the basis of results obtained for nanodrops and some experimental results are interpreted. The main conclusion is that the hidden roughness has a similar effect on the drop features as the traditionally considered physical and chemical roughnesses.

1 Introduction

For a long time, a liquid drop on the surface of a solid was the object of intense experimental and theoretical investigations and numerous results were obtained using various methods. Particular attention was given to rough surfaces because of the large effect

which roughness has on the wetting of a solid substrate. Two kinds of roughnesses were considered. One of them is due to the asperities present on the surface of a homogeneous solid substrate (physical rouhgness). The second, chemical roughness, occurs when the substrate has a smooth surface with nonuniform chemical composition. For both types of roughnesses, the contact angle of the drop on the rough surface is usually greater than on the smooth one, i.e. the roughness increases the hydrophobicity.[1,2] Another important feature of a rough surface, which is absent for a smooth one, is the appearance of the sticking (pinning) of the drop-solid contact line to the solid surface due to the direct contact of this line with the asperities (see e.g. Ref. 3).

In the present paper, a new type of roughness, which will be called as hidden roughness, is considered using a microscopic approach based on the density functional theory (DFT). The system which possesses such a roughness, can be imagined, for instance, as a uniform substrate decorated with asperities (SDA) and covered by a layer of a second solid material (SSM) which has a smooth surface but can have a nonuniform density. The drop on the smooth surface of SSM is subjected to the interaction potentials of SDA and SSM, which determine its properties. The contact angle of the drop is expected to depend on the details of the fluid-solid interactions and nonuniformity of SSM. Another expectation is that if an external force acts on the drop parallel to the surface, the SSM and SDA will generate a sticking force which maintains the equilibrium of the drop on the surface. The presence of only one kind of liquid in the system (that of the drop) allows one to use for its study the one-component DFT developed in Ref. 4.

As an example of a real system possessing hidden roughness, one can mention the

Figure 1: (a) Schematic representation of the drop on an inclined rough substrate (black area) covered with a lubricating liquid. $\mathbf{F}_{g,\tau}$ is the component of gravity parallel to the surface of the lubricating liquid and $\mathbf{F}_{st}$ is the sticking force which maintains the drop equilibrium. (b) Contact angles at advancing (θ_1) and receding (θ_2) leading edges of the drop.

recently examined systems involving the slipping of a drop on inclined surfaces.[5–12] The main idea consisted in filling the space between asperities of a textured surface with a lubricating liquid which adheres to the substrate, and place a drop of the test liquid on the surface of the lubricating liquid (see Fig. 1). In Fig. 1a, $\mathbf{F}_{g,\tau}$ is the component of gravity along the surface and $\mathbf{F}_{st}$ is the sticking force which provides the mechanical equilibrium of the drop. The angles θ_1 and θ_2 in Fig. 1b are the contact angles of the advancing and receding edges of the drop. The drop is in mechanical equilibrium until $\alpha \leq \alpha_c$, α_c being a critical angle. For $\alpha > \alpha_c$ the drop slips or rolls along the surface. For $\alpha = \alpha_c$ the sticking force acquires the critical value $F_{st,c}$ and angles θ_1 and θ_2 become θ_a (advancing contact angle) and θ_r (receding contact angle), respectively. When the test and lubricating liquids

are immiscible the surface of the lubricating liquid is smooth and the drop can slip along the surface at very small inclinations ($\alpha \sim 3^\circ$). The name SLIPS (slippery liquid-infused porous surface) was given to such a system.[5]

The main difference between SLIPS and the system considered in this paper is that in the former case the drop of the test fluid is in contact with another, lubricating, liquid but not with SDA. Because of the presence of two different fluids, the one-component DFT can not be directly applied to such a system and more sophisticated and time-consuming versions of DFT must be used. In spite of this, one can mimic SLIPS using particular choices for SSM such as the nonuniform density distribution and the interaction parameters with the drop. In this case the one-component DFT can provide, to some extent, a microscopic insight for SLIPS.

Note that the DFT approach has the advantage that it does not involve any phenomenological parameters and accounts explicitly for the microscopic details of the fluid-fluid and fluid-solid interactions. This allows to consider nanosystems to which macroscopic concepts, such as surface tension, are not applicable. As a disadvantage of DFT one can mention the extremely large computational time necessary to obtain results for macroscopic drops that makes such calculations impractical. However, there are cases in which one can extract some information about macroscopic drops from results obtained for nanodrops. An example is the cylindrical drop, i.e. a very (infinitely) long drop, which is frequently used in considerations regarding wetting phenomena (see Ref. 13 and references therein). The contact line of such a drop is a straight line, which does not depend on the drop size. If the interactions of the drop molecules with those of the SDA

and SSM decrease sufficiently rapid with increasing distance between molecules one can expect the critical sticking force acting on the drop at the contact line to be the same for macro- and nanodrops if the two contact lines have identical locations on the surface with respect to the horizontal profile of the fluid-solid interaction potential. The critical sticking force for a nanodrop can be calculated using DFT in a way described in Ref. 14 and this value is used for the sticking force of a macrodrop.

The two goals of the present paper are (i) to examine the new kind of roughness and its influence on the contact angle and sticking force for a drop located on the surface of such a solid, and (ii) to estimate the sticking force for macroscopic drops using results from nanodrops. Because the force of gravity is extremely small for nanodrops, it cannot break their mechanical equilibrium even when the drops are on a vertical surface with $\alpha = 90°$.[14] To obtain information about the sticking force, we will consider a nanodrop on a horizontal surface and apply a perturbative horizontal force f_τ on each molecule of the drop. By changing f_τ, a critical value $f_{\tau,c}$ can be found such that for $f_\tau > f_{\tau,c}$ the Euler-Lagrange equation of DFT, which provides the equilibrium state of the system, has no drop-like solution. Then the critical sticking force $F_{st,c}$ is provided by $F_{st,c} = N_d \times f_{\tau,c}$, where N_d is the number of molecules in the drop, which can be found from the solution of the Euler-Lagrange equation of DFT. For the sake of generality, in the present paper no specific fluids, liquids, and surfaces are considered, but the parameters of intermolecular interactions are selected from reasonable ranges.

Note that in experiments involving inclined surfaces, the magnitude of the critical

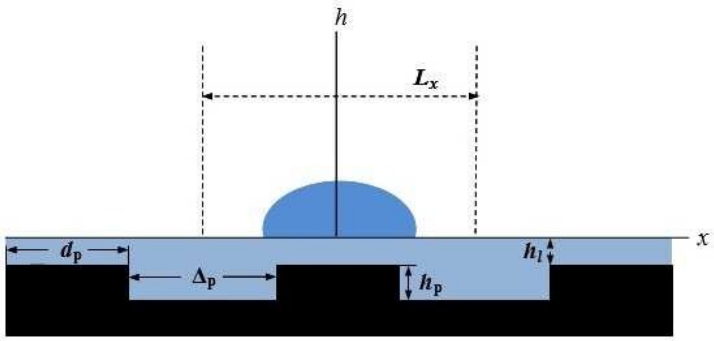

Figure 2: Schematic representation of the considered system which consists of a solid (substrate and pillars) of constant density (black area) covered by a second solid material (SSM) (light area), and the drop of the test fluid on the smooth surface of SSM. The lengths d_p, h_p, and Δ_p are the pillars width, pillars height, and distance between pillars, respectively, h_l is the thickness of SSM above the pillars, $L_x = d_p + \Delta_p$ is the width of the unit cell used in the calculations. All distances between surfaces are measured between the centers of the molecules forming the first layers of the corresponding surfaces. The x-axis passes through the centers of molecules of the test fluid located at the bottom surface of the drop.

sticking force $F_{st,c}$ on a drop of mass M can be easily found using the equation

$$F_{st,c} = Mg \sin \alpha_c \ . \tag{1}$$

2 General considerations

2.1 The system

2.1.1 Geometry

The considered system consists of three components which are presented in Fig. 2. The first component, SDA, (black area in Fig. 2) is a semiinfinite substrate of constant density

ρ_s decorated with regular arrays of pillars of height h_p, width d_p and distance between pillars Δ_p. All distances between surfaces are measured between the centers of the molecules of their first layers. The pillars are infinite in the y-direction (normal to the plane of the figure) and composed of the same material as the substrate. The second solid material (SSM) (lighter area) fills the space between pillars and forms a layer of thickness h_l above them which has a smooth upper surface. The density of SSM is considered nonconstant and will be provided in Sec. 2.1.4. The third component is a test fluid (TF) which forms a drop on the surface of SSM. The drop is in thermodynamic equilibrium with its vapor. Note that the density distribution of SSM is considered independent of the density distribution of TF.

The upper boundary of the system (not shown in Fig. 2), located at distance h_u from the surface of SSM, is treated as a hard wall. Because of the low density of TF outside the drop, the influence of the upper boundary on the state of the system can be neglected. In the x- direction, the system is considered periodic with period L_x, the number of molecules of TF per L_x being constant (closed system).

The density distribution (FDD) of TF, $\rho_f(\mathbf{r})$, in this system is considered uniform in the y-direction (cylindrical drop) and non-uniform in the x- and h-directions, hence $\rho_f(\mathbf{r}) \equiv \rho_f(x, h)$. The test fluid is exposed to an external potential due to the TF-SDA and TF-SSM interactions.

2.1.2 Interaction potentials

The interaction potentials between the molecules of TF and those of TF, of SSM and SDA are selected in the Lennard-Jones form with hard core repulsion

$$\phi_\alpha(|\mathbf{r}-\mathbf{r}'|) = \begin{cases} 4\epsilon_\alpha\left[\left(\frac{\sigma_\alpha}{r}\right)^{12}-\left(\frac{\sigma_\alpha}{r}\right)^{6}\right], & r \geq \sigma_\alpha \\ \infty, & r < \sigma_\alpha \end{cases} \quad (2)$$

where the subscript α should be ff, fm, and fs for the TF-TF, TF-SSM, and TF-SDA interactions, respectively, ϵ_{ff}, ϵ_{fm}, and ϵ_{fs} are energy parameters, σ_{ff}, σ_{fs}, and σ_{fm} are hard core diameters of the corresponding interaction potentials, $\mathbf{r}$ and $\mathbf{r}'$ provide the locations of the interacting molecules, and $r = |\mathbf{r}-\mathbf{r}'|$.

Because of the geometry of the system, the external potential $U_{fs}(\mathbf{r})$ generated by the substrate and pillars depends on x and h and is independent of y, i.e. $U_{fs}(\mathbf{r}) \equiv U_{fs}(x,h)$. Due to the ordered geometrical location of the pillars and uniformity of the substrate, this potential is periodic in the x-direction with period L_x. The potential $U_{fs}(\mathbf{r})$ can be obtained by integrating the Lennard-Jones potential (eqn (2)) for the TF-SDA interactions over the entire volume of SDA and can be written as

$$U_{fs}(\mathbf{r}) = \int_{V_s} \rho_s(\mathbf{r}')\phi_{fs}(|\mathbf{r}-\mathbf{r}'|)d\mathbf{r}' + \int_{V_p} \rho_s(\mathbf{r}')\phi_{fs}(|\mathbf{r}-\mathbf{r}'|)d\mathbf{r}' \quad (3)$$

where V_s is the volume occupied by the substrate, V_p is the volume occupied by the pillars, $\rho_s(\mathbf{r}')$ is the density of SDA. For a uniform SDA, $\rho_s(\mathbf{r}') \equiv \rho_s$, and the first integral in eqn (3) can be calculated analytically

$$\int_{V_s} \rho_s(\mathbf{r}')\phi_{fs}(|\mathbf{r}-\mathbf{r}'|)d\mathbf{r}' = \frac{2\pi}{3}\epsilon_{fs}\rho_s\sigma_{fs}^3\Psi(\sigma_{fs}, h_l + h_p + h) \ . \tag{4}$$

where $\Psi(\sigma, H) = \frac{2}{15}\left(\frac{\sigma}{\sigma+H}\right)^9 - \left(\frac{\sigma}{\sigma+H}\right)^3$.

In the second integral in eqn (3), the integration with respect to y could be performed analytically. Integration with respect of x- and h-coordinate was carried out numerically.

The contribution $U_{fm}(\mathbf{r})$ of SSM to the total potential is provided by equation

$$U_{fm}(\mathbf{r}) \equiv U_{fm}(x,h) = \int_{V_m} \rho_m(\mathbf{r}')\phi_{fm}(|\mathbf{r}-\mathbf{r}'|)d\mathbf{r}', \tag{5}$$

where V_m is the volume occupied by SSM, and depends on the density distribution $\rho_m(\mathbf{r}) \equiv \rho_m(x,h)$. The choice of $\rho_m(x,h)$ is explained in Sec. 2.1.4. As for the case of TF-SDA potential, the integration with respect to y in eqn (5) could be performed analytically and with respect to x- and h- coordinates, numerically.

A perturbative horizontal force f_τ acting on a molecule of TF in the negative direction of the x-axis generates the potential

$$U_e(\mathbf{r}) \equiv U_e(x) = f_\tau x \tag{6}$$

which is zero in origin.

Finally, the net potential has the form

$$U_{net}(x,h) = U_{fs}(x,h) + U_{fm}(x,h) + U_e(x) \ . \tag{7}$$

2.1.3 Parameters of the substrate and pillars, and test fluid

Below, the lengths will be provided in units of TF-TF hard core diameter, σ_{ff}. The following geometrical characteristics of the system were selected as constants: $h_p = 4$, $d_p = 2$, $\Delta_p = 6$, and $h_u = 20$. The small size of asperities was selected to decrease the computational time. Comparable or even smaller sizes are often used in molecular dynamics simulations (see e.g. Ref. 15). Three thicknesses of SSM were considered. They are characterized by the thicknesses of that part of SSM which is above the pillars and were selected as $h_l = 1$ (system S1), $h_l = 3$ (system S2), $h_l = 10$ (system S3). The parameters of the interaction potential for TF-TF interactions were selected as for argon[16] : $\sigma_{ff} = 3.405$Å, $\epsilon_{ff}/k_B = 119.76$K, where k_B is the Boltzmann constant. For TF-SDA and TF-SSM interactions the energy parameters were selected as $\epsilon_{fs}/k_B = 145$K and $\epsilon_{fm}/k_B = 135.8$K, respectively. The reason for such a selection will be explained in Sec. 2.1.4. The hard core diameters for those interaction potentials were considered equal ($\sigma_{fs} = \sigma_{fm} = \sigma_{ff}$). The temperature was selected $T = 87.3$K, that is far from the critical temperature of bulk TF ($T_c = 131.6$K)[16] . For this reason one can neglect the critical density fluctuations and the mean-field DFT can be employed to describe the selected system. The number density of SDA was selected $\rho_s = 1.91 \times 10^{28}\text{m}^{-3}$ and the mass of a molecule of TF $m_f = 6.63 \times 10^{-26}$kg.

2.1.4 Selection of the second solid material (SSM)

As mentioned in the Introduction, the system considered in the present paper can mimic SLIPS by using a particular choice of SSM instead of the lubricating liquid (LF) of SLIPS.

To make this choice, two auxiliary systems were considered. The goal was (i) to select an LF which is immiscible with TF and (ii) to determine the density distribution of that LF in contact with a rough solid and use it as the density distribution of SSM.

To select a suitable LF, the system consisting of a smooth substrate in contact with a mixture of LF and TF was considered first using the density functional approach formulated by Rosenfeld[17] for binary mixtures. The substrate and TF were the same as those described in Sec. 2.1.3. The applied calculational procedure is similar to that used in Ref. 18 where a binary mixture in contact with a uniform solid was considered. However, in the present calculations the system is considered connected to the reservoir of TF at a chemical potential equal $-12.5k_BT$ (open system). Analyzing the density distributions of TF and LF for various values of the parameters of LF (σ_{ll}, ϵ_{ll}, and ϵ_{ls}) the latter quantities were selected as follows: $\sigma_{ll} = \sigma_{ff}$, $\epsilon_{ll}/k_B = 194$K, and $\epsilon_{ls}/k_B = 220$K. This choice of parameters provides an example of a suitable LF. Finally, the same parameters were used in a second auxiliary system, consisting of a rough solid and LF, to find the density distribution of LF in contact with a rough surface using the one-component DFT[4]. The obtained density distribution (FDD), $\rho_l(x, h)$, is presented in Fig. 3 for the system $S1$. In Fig. 3a, the FDD in the x-direction is provided for the range between pillars. One can see that the space between pillars is filled with the "liquid-like" LF. The FDD in the x-direction above the pillars is presented in Fig. 3b. As expected, the amplitude of the density oscillations decreases with increasing distance from SDA. The FDD in the vertical direction is presented in Fig. 3c along the line passing through the midway between pillars (solid line) and the line passing in the middle of a pillar. Finally, the part of this

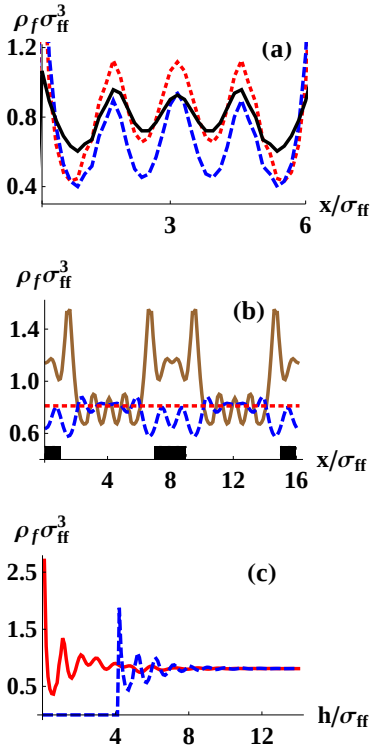

Figure 3: System $S1$. (a) Density distribution of LF between the solid pillars at various distances h from the surface of the substrate: $h = 1$ (dotted line), $h = 2.5$ (dashed line), and $h = 4$ (solid line); (b) Density distribution of LF above the solid pillars at various distances h from their upper surfaces: $h = 0.3$ (solid line), $h = 1$ (dashed line), and $h = 10$ (dotted line). The rectangles in the bottom part show the locations of the solid pillars.; (c) Density distribution of LF along the vertical lines passing through the midway between pillars (solid line) and through the middle of the pillars (dashed line).

distribution for a thickness equal to that of SSM was extracted and used to calculate the potential $U_{fm}(x,h)$ with eqn (5), where $\rho_m(x,h) = \rho_l(x,h)$.

Another feature which should characterize SSM is its wetting temperature T_w, which should be higher than the selected T=87.3K because only in this case the drop is stable on the surface. To find T_w, the open system consisting of uniform SSM in contact with TF was considered and the wetting temperature estimated using the method described in Ref. 19. It turned out that the wetting temperature of considered system is greater than 100K and hence, the selected temperature is suitable.

2.2 The Euler-Lagrange equation for the fluid density distribution

To find the FDD of the test fluid (TF), $\rho_f(x,h)$, the weighted density approximation (WDA) version of the DFT suggested first in Ref. 20 and developed further in Ref. 4 was used. This version of DFT accounts for the non-local, short-ranged correlations in the fluid and provides the correct structure of fluids near solid walls. The equation for the FDD of TF, $\rho_f(x,h)$, is obtained through the minimization of the total Helmholtz free energy $F[\rho_f(\mathbf{r})]$ of the system under the constraint of a constant number of molecules, i.e. in a canonical ensemble (see Appendix). Such a procedure was developed in Refs. 21-24 and provided the convergence of the numerical iterations to drop-like solutions. The Euler-Lagrange equation can be represented in the form

$$\log[\Lambda^3 \rho_f(x,h)] - Q_f(x,h) = \frac{\lambda}{k_B T} \tag{8}$$

where the function $Q_f(x,h)$, which is a functional of $\rho_f(x,h)$, is provided in Appendix (eqn (A. 8)), $\Lambda = h_P/(2\pi m_f k_B T)^{1/2}$ is the thermal de Broglie wavelength, h_P is the Planck constant, and λ is a Lagrange multiplier arising because of the constraint of fixed average density of the fluid. This constraint has the form

$$\rho_{f,av} = \frac{1}{V} \int_V d\mathbf{r} \rho_f(\mathbf{r}) \tag{9}$$

where V is the volume occupied by TF, and leads to the following expression for λ

$$\lambda = -k_B T \log \left[\frac{1}{\rho_{f,av} V' \Lambda^3} \int_{V'} d\mathbf{r} e^{Q_f(x,h)} \right]. \tag{10}$$

In the above equation, $V' = L_x h_u$ is the volume per unit length in y-direction occupied by TF. By eliminating λ between eqn (8) and eqn (10), one obtains an integral equation for the FDD $\rho_f(x,h)$, which can be solved by iterations. When calculating the density distribution $\rho_f(x,h)$ of TF, the net potential is provided by the sum of $U_{fs}(x,h)$, $U_{fm}(x,h)$, and $U_e(x,h)$ the latter two being calculated with eqn (5) and eqn (6).

The main details of the iteration procedure are provided in Refs. 14,25 and in the Appendix where a calculation tactic, that considerably reduce the time to find the numerical solution of the Euler-Lagrange equation for the density distribution of the test fluid, is presented.

The procedure described in the present section, was also employed to find the FDD of

the lubricating fluid in contact with a rough solid. The latter FDD is used to model the nonuniform SSM (see Sec. 2.1.4).

2.3 Calculation of the drop profile

Because of the relatively large width of the vapor-liquid interface detected in molecular dynamics experiments as well as in DFT calculations,[25,26] the profile of the nanodrops is not clearly defined. There are several approaches to extract the profile from a known FDD (see Refs. 26,27 as examples). In this paper we use the simplest one employed in Ref. 27 and determine the profile inside the vapor-liquid interface as that corresponding to a constant local density ρ_{div} which can be defined as the density for an equimolar dividing surface of a horizontal FDD $\rho(x, h_0)$ at some distance h_0 from the surface, by considering this FDD as that of a planar vapor-liquid interface[25] To select the most appropriate value of h_0, one should note, that for $h < 3\sigma_{ff}$ the fluid density distribution $\rho_f(x, h)$ inside the drop has an oscillatory behavior as a function of h (because the fluid molecules form several liquid layers of various densities)[28] and as a function of x (due to the roughness of the surface). For these reasons, it is not clear how to determine ρ_{div} for $h_0 < 3\sigma_{ff}$. For $h_0 > 3\sigma_{ff}$ those oscillations become smaller and FDD $\rho_f(x, h_0)$ ($h_0 > 3\sigma_{ff}$) exhibits a clearly observable interface between high and low density phases, for which one can easily find ρ_{div} and define a dividing surface for the selected h_0. Hence, it is reasonable to select a value of h_0 larger than $3\sigma_{ff}$.

After the profile is determined, other characteristics of the drop, such as the advancing and receding contact angles and the number of molecules in the drop can be calculated[25]

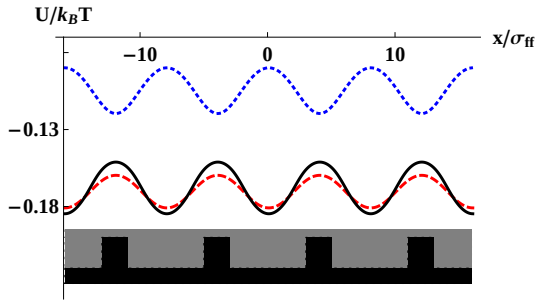

Figure 4: TF-SSM interaction potential in the system $S1$ for a nonuniform (solid line) and uniform (dashed line) SSM. The potential is calculated at distance σ_{ff} from the surface of SSM. The dotted line is the net potential of substrate and pillars. For clarity, it is multiplied by a factor of 10. The insert beneath the plots indicates the locations of the pillars.

3 Results

3.1 Potentials of intermolecular interactions

In Fig. 4, the potential $U_{fm}(x,h)$ generated in the system $S1$ by a nonuniform SSM at distance σ_{ff} from the SSM surface ($h=0$) is presented (by the solid line) as function of x. The nonuniform density $\rho_m(x,h)$ of SSM was calculated as described in Sec. 2.2 and $U_{fm}(x,h)$ was obtained using eqn (5). To estimate the role of nonuniformity of SSM, the potential generated by a uniform SSM with the same average density as the nonuniform SSM ($\rho_{av}\sigma_{ff}^3 \simeq 0.82$) is presented as a dashed line. As expected, both potentials are periodic with respect to x with a period $L_x = \Delta_p + d_p$. The periodicity of the potential generated by the uniform SSM is due to the presence of "upside down pillars" of SSM regularly located between the pillars on the substrate, whereas the layer above them produces a uniform potential. For the nonuniform SSM considered below, the nonuniformity

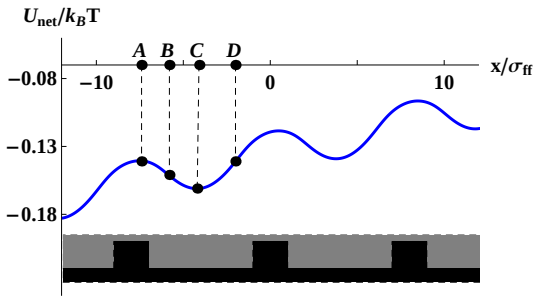

Figure 5: Net potential as function of x for $h = 0$ in system $S1$. The extrema of the potential have labels A and C and the inflection points are marked with B and D.

of the potential is caused both by the pillars of SSM and by the nonuniformity of the density distribution, $\rho_m(x, h)$. One can see in Fig. 4, that the amplitude of the changes of $U_{fm}(x, h)$ is slightly larger for a nonuniform SSM than for a uniform one, while their magnitudes differ very little. In both cases, the minima of $U_{fm}(x, h)$ as function of x are located on the vertical lines of symmetry of the pillars of SSM.

The potential $U_{fs}(x, h)$, generated by the substrate and pillars located on its surface, behaves similarly to $U_{fm}(x, h)$, the minima of the potential being displaced by $(\Delta_p + d_p)/2$ with respect to those of $U_{fm}(x, h)$. The magnitude of U_{fs} at $h = 0$ is much smaller than that of U_{fm} due to the larger distance from the substrate.

In Fig. 5, the net potential $U_{net}(x, h)$ provided by eqn (7), is presented as function of x for the system $S1$. In this example, the horizontal force f_τ in the negative x-direction on a single molecule of TF was 9.7×10^{-15}N. The total potential possesses multiple minima separated by potential barriers; due to the presence of the perturbative force f_τ the local minima of the potential gradually increase with increasing x.

Because of the periodicity of the potentials $U_{fs}(x, h)$ and $U_{fm}(x, h)$ in the x direction,

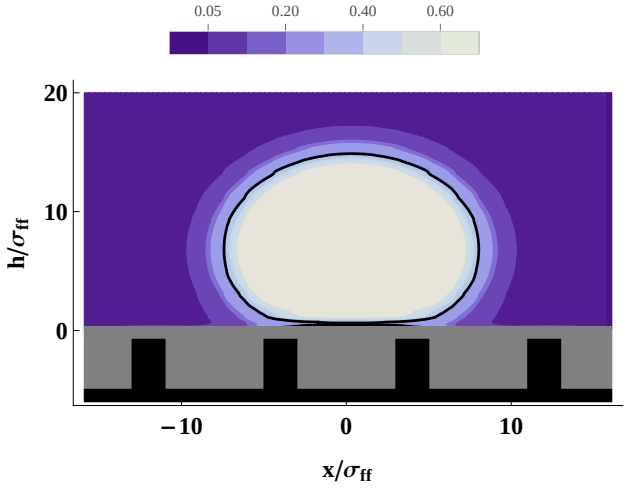

Figure 6: Example of a drop on the surface of SSM for the system $S1$. The solid line presents the drop profile. The magnitude of the fluid density is provided in dimensionless form as $\rho\sigma_{ff}^3$.

any drop, in the absence of the horizontal perturbative force f_τ, has the same free energy when it is displaced along the surface over an integer number of periods. However, in the presence of that force, the potential energy of the drop decreases if the drop is displaced in the negative x-direction. This means that any drop on a surface is metastable.

3.2 Drop profile and contact angle

In Fig. 6, a typical drop of the system $S1$ is presented in the absence of the external perturbative force ($f_\tau = 0$). The size of the drop (number of molecules per unit length in y-direction) $N_d = 2.82 \times 10^{11}1/\text{m}$. The drop profile, determined as described in Sec. 2.3, is provided by the solid line. The densities given on the legend bar above the figure are provided in dimensionless form as $\rho\sigma_{ff}^3$. The drop is symmetrical with respect to the vertical line passing midway between solid pillars. Note that another solution, which is

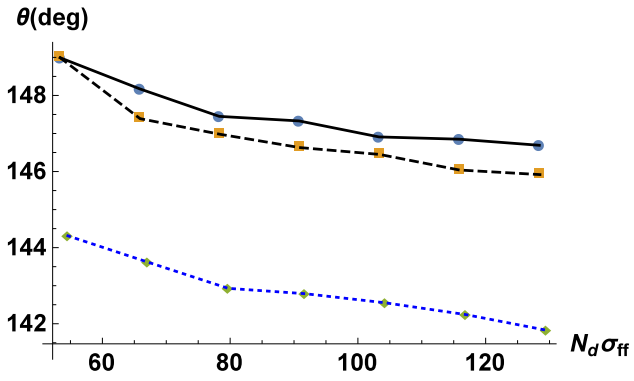

Figure 7: Calculated dependence of θ on the drop size in the absence of external force ($f_\tau = 0$) for systems S1 (diamonds), S2 (squares), and S3 (points) The lines are guides for eye.

symmetrical with respect of the middle of the solid pillars, was also identified; however the free energy of this solution is greater that of for the drop from Fig. 6. However, the analysis of its stability by the method described in Appendix, did not provide unambiguous proof of whether this solution is metastable or unstable. The lack of evidence may be due to the very small height of the potential barrier (if the drop is, actually, metastable) or because the extremum of the free energy obtained by solving the Euler-Lagrange equation is a maximum (unstable drop). Because of this, only the stable drops (with smallest free energies) will be presented below.

In the absence of the external force ($f_\tau = 0$), the left and right parts of the drop profile make the same angles with the surface ($\theta_1 = \theta_2 = \theta$). The magnitude of θ depends, in particular, on the size of the drop. In Fig. 7, this dependence is presented for all three considered systems. In all cases, the contact angle decreases with increasing size of the drop. For the same size, the drop of the system $S1$ has the smallest and in $S3$, the largest contact angles.

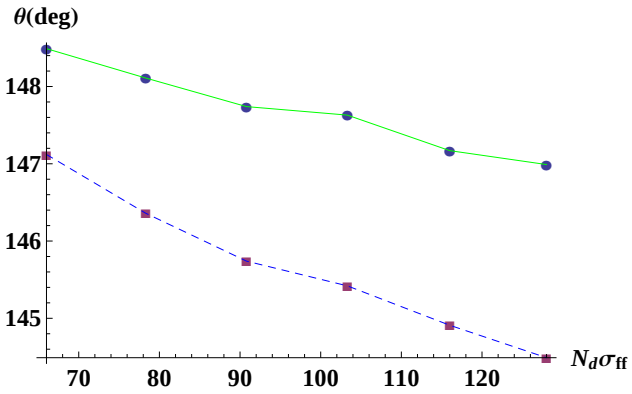

Figure 8: System S2. Calculated dependence of θ_1 (points) and θ_2 (squares) on the number N_d of molecules of the test fluid in the drop for $f_\tau = 2.92 \times 10^{-16}$N. The lines are guides for eye.

The size dependence of θ for nanodrops was examined earlier in several studies using DFT[25,29,30] or molecular dynamics simulations[31] but till now no universal explanation of this dependence was found.

One of the possible explanations involves the concept of line tension introduced in Ref. 32 which leads (for three dimensional drops) to an additional term in the Young equation containing the reciprocal of the radius of the contact line between drop and solid surface. However, for the cylindrical drop considered in the present paper, the line tension can not explain the size dependence of θ because the contact line is a straight line ($R = \infty$) and the additional term in Young equation disappears. Even more, the Young equation itself and its modifications suggested in Refs. 33,34 are not applicable to nanodrops because they are based on macroscopic considerations involving surface tensions, the latter quantities are not clearly defined at the nanoscale. A possible explanation of this dependence for the considered case will be provided in Discussion.

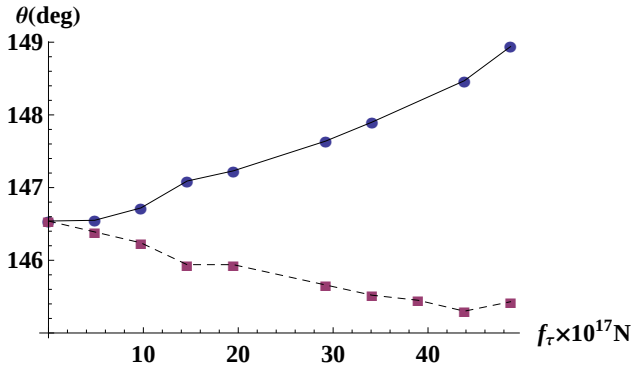

Figure 9: Calculated dependence of θ_1 (points) and θ_2 (squares) on f_τ. The lines are guides for eye.

In the presence of an external perturbative force ($f_\tau \neq 0$) in the negative x direction, $\theta_1 \neq \theta_2$ and both angles depend on the size of the drop. An example of this dependence is presented in Fig. 8 for the system $S2$ and $f_\tau = 2.92 \times 10^{-16}$N. The N_d dependence is close to linear and both angles decrease with increasing N_d.

At constant size of the drop, the angles θ_1 and θ_2 depend on f_τ. This dependence is presented in Fig. 9 for the system S2. For all values of f_τ, the number of molecules in the drop per unit length is the same ($N_d \simeq 2.85 \times 10^{11}$). The angle θ_1 increases and θ_2 decreases with increasing f_τ. As a consequence, the difference between these angles increases with increasing external force.

To estimate the influence of SSM inhomogeneity on the contact angle, the latter was calculated for the same drop on the surface of nonuniform and uniform SSM. At $f_\tau = 0$, the contact angle of the drop containing 2.82×10^{11} molecules per unit length is 150.62° and 149.73° for the nonuniform and uniform SSM, respectively. The contact angle on nonuniform SSM is slightly larger than that on the uniform SSM, in agreement with

general ideas about the influence of roughness on the contact angle.

3.3 Sticking force

The shape of the net potential allows one to explain qualitatively the microscopic origin of the sticking force acting on a drop of TF, which arises due to the interaction of the fluid molecules with a smooth nonuniform SSM that covers the rough solid. The basic idea is that the main contributions to the sticking force comes from the forces imposed on the molecules located at both leading edges of the drop.[35–37] When the leading edge (advancing or receding) of the drop on the SSM surface is located between points A and C of Fig. 5,[1] the potential $U_{net}(\mathbf{r})$ generates a force on the molecules of the drop at the leading edge in the positive direction of the x axis, which opposes the motion of the drop in the negative x-direction along the surface due to the external force $\mathbf{F}_{ext}$. Only a large enough perturbative force can overcome the potential barrier and set the drop in motion. The magnitudes of the components of the sticking force at any of the two leading edges are proportional to the x-components of the gradient of the net potential at the location of the leading edges with respect to the potential profile. Each of them increases when the leading edge is displaced in the direction from point C to point B (see Fig. 5) and decreases when it is displaced from point B to point A.

Tables 1 and 2 list the values of the critical sticking forces $F_{st,c}$ and contact angles obtained for systems $S1$, $S2$, and $S3$ for several situations. In addition, the weight of the nanodrop and the contact angle hysteresis $\Delta\theta = \theta_{a,c} - \theta_{r,c}$ are also presented. Comparing

[1] "Between points A and C" means all similar ranges of the potential curve.

Table 1: Critical sticking force for the drop containing about 2.84×10^{11} molecules per unit length for all considered systems. $\theta_{a,c}$ and $\theta_{r,c}$ are the advancing and receding contact angles, respectively, Mg is the weight of a drop per unit length, $\Delta\theta$ is the contact angle hysteresis.

System	$F_{st,c}(\mu N/m)$	$\theta_{a,c}(deg)$	$\theta_{r,c}(deg)$	$Mg(pN/m)$	$\Delta\theta(deg)$	$N_d\sigma_{ff}$
$S1$	151	149.66	146.01	0.185	3.65	96.8
$S2$	140	148.90	145.43	0.185	3.47	96.9
$S3$	99.3	143.80	141.64	0.188	2.16	98.5

Table 2: Critical sticking force for the drops containing various numbers of molecules per unit length for the system S2. $f_{st,c}$ is the critical sticking force per molecule. Other notations are the same as in Table 1.

$N_d\sigma_{ff}$	$F_{st,c}(\mu N/m)$	$f_{st,c} \times 10^{14} N$	$\theta_{a,c}(deg)$	$\theta_{r,c}(deg)$	$Mg(pN/m)$	$\Delta\theta(deg)$
66.0	131	4.46	149.20	147.30	0.126	1.90
96.9	140	4.77	148.90	145.43	0.185	3.47
127.1	99.3	2.44	143.80	141.64	0.188	2.16

the results listed in Table 1, one can mention, first, that for the drop of approximately the same size the magnitude of the sticking force decreases with increasing thickness of the SSM above the pillars. This is an obvious consequence of the decreasing influence of the inhomogeneity of the SDA and SSM in the x-direction because of the increasing distance of the smooth surface from the pillars on the surface of the substrate.

The second interesting observation is that increasing of the size of the drop can lead to opposite results for the sticking force. For example (see Table 2), when the drop size

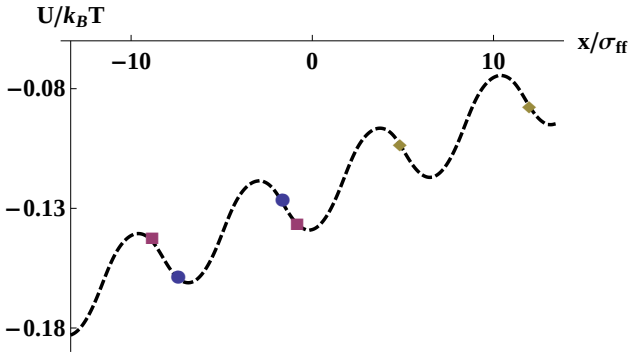

Figure 10: System S2. Location of the leading edges, with respect to the net potential, of critical drops for $N_d\sigma_{ff} = 66.0$ (points), 96.9 (diamonds), and 127.1 (squares).

increases from $N_d\sigma_{ff} = 66.0$ to $N_d\sigma_{ff} = 96.9$ the sticking force increases from 131μN/m to 140μN/m. However a further increase of the size to $N_d\sigma_{ff} = 127.1$ leads to the decrease of the sticking force to 99.3μN/m. To explain such a behavior of $F_{st,c}$, one should note that the drop size affects the locations of the leading edges of the drop. In Fig. 10 those locations are presented schematically with respect to the net potential generated by SSM and SDA. The points present the location of the leading edges of the drop with $N_d\sigma_{ff} = 66.0$, diamonds and squares correspond to drops with $N_d\sigma_{ff} = 96.9$ and $N_d\sigma_{ff} = 127.1$, respectively. One can see that both leading edges of the drop with $N_d\sigma_{ff} = 96.9$ are located close to the points with the largest slope of the potential curve, i.e. the sticking force is close to the maximum possible. The leading edges of the drop with $N_d\sigma_{ff} = 127.1$ are located close to the points with the smallest slope of the potential curve. As a consequence, the sticking force for this drop is smaller than for the previous one. For the drop with $N_d\sigma_{ff} = 66.0$, the advancing leading edge is located close to the point with the smallest slope and the receding leading edge close to the point with the

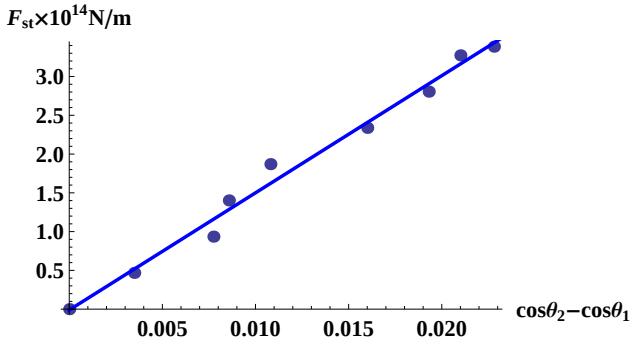

Figure 11: System $S3$. Dependence of the sticking force on the difference $\cos\theta_2 - \cos\theta_1$. Points are results of calculations, line is the best linear fit. θ_1 and θ_2 are defined in Fig. 1.

largest slope. The magnitude of the sticking force has in this case an intermediate value when compared with has two above considered drops.

It is interesting to compare the results obtained for the sticking force for nanodrops with the predictions made on the basis of the traditional macroscopic approach. The latter provides for the sticking force the equation

$$F_{st} = C\gamma_{lv}(\cos\theta_2 - \cos\theta_1) \tag{11}$$

where θ_1 and θ_2 are defined in Fig. 1, γ_{lv} is the liquid-vapor surface tension and C is a constant dependent on the geometry of the drop.[38,39] In Fig. 11, the dependence of the sticking force on $\cos\theta_2 - \cos\theta_1$ is presented for the system $S3$. One can see that the F_{st} calculated on the basis of DFT can be reasonable approximated by eqn (11).

Comparing the values of $F_{st,c}$ and Mg listed in Tables 1 and 2 one can see that the weight of a nanodrop is much smaller that the sticking force acting on it. This means that the gravity alone cannot overcome the sticking force even for $\alpha = 90^\circ$ (vertical wall).

However, the results obtained for nanodrops allow to estimate an upper bound for the critical inclination angle, α_c, for macroscopic cylindrical drops on an inclined surface. As noted in the Introduction, this can be achieved because the leading edges of macro- and nanodrops are identical for cylindrical drops. For this reason, the sticking force on a cylindrical drop of any size depends only on the location of the leading edges with respect to the interaction potential profile. Considering nanodrops of different sizes on the surface of the lubricating liquid, which have various locations of the leading edges, the largest sticking force $F_{st,c}$ on the nanodrops can be obtained and associated with the largest possible sticking force acting on a macrodrop. If the latter has a mass M_d, then the largest inclination angle α_c at which the macrodrop is at rest can be calculated from eqn (1) as $\sin\alpha_c = F_{st,c}/M_d g$. For example, let us consider in the system $S3$ a cylindrical drop of liquid argon of volume $v = 1\mu L/\text{cm}$. Such a drop contains about 2×10^{21} molecules/m and has a weight $M_d g \simeq 1.4\text{mN/m}$. For estimation of the inclination angle α_c, the largest calculated sticking force $F_{st,max} = 99.3\mu\text{N/m}$ will be selected. In this case, α_c is equal to about 4.1°, i.e. close to the inclination angles observed in SLIPS experiments. The largest inclination angle α_c will decrease (increase) with increasing (decreasing) mass of the macrodrop.

4 Discussion

The results obtained in the present paper show that the hidden roughness has qualitatively the same influence on the behavior of a nanodrop as the physical and chemical roughnesses

of the solid surface. Namely, the hidden roughness increases the hydrophobicity of the solid and generates the sticking force.

The microscopic picture of a drop on the surface in the presence of roughness developed in Refs 14,25 and in the present paper shows, in particular, that the sticking force and contact angle depend on different characteristics of the interaction potential. While for the same geometrical characteristics of the solid, the potential contributes mainly to the contact angle θ,[13] the sticking force is affected mainly by the slope of the horizontal profile of the interaction potential at the locations of the leading edges of the drop. If this slope is large, the sticking force can be large even for superhydrophobic surfaces. For small variation of the interaction potential in the horizontal direction, the sticking force can be extremely small. The difference between the potential profiles may be the reason of the difference between the adhesive properties of the surfaces of the rose petal and lotus leaf.[40] Both surfaces are superhydrophobic ($\theta \geq 150^\circ$), but the first one possesses a large contact angle hysteresis and a sticking force that prevents slipping even at high inclination angles, while the second has a small contact angle hysteresis and a small sticking force. The liquid drop on the lotus leaf can easily roll down at very small inclination angles α. Detailed analysis which is needed to check this suggestion is not of concern in the present paper.

The nonuniformity in the horizontal direction of the interaction potential due to the hidden roughness and the appearance of the sticking force it causes can qualitatively explain the dependence of the contact angle θ on the size of the drop. Indeed, the presence of the sticking force opposes (to some extent) the expansion of the drop base with

increasing drop size which leads to the increase of θ. On the other hand, the displacements of the leading edges with respect to the profile of the interaction potential can lead to the decrease of the sticking force and, as a consequence, to the increase of the drop base and decrease of the contact angle. As a result, the contact angle can decrease or increase with increasing size of the drop. The actual change of θ can be found only by calculations.

The method used in the present paper to find the conditions of breaking equilibrium of a drop in the presence of the external perturbative force can not provide an answer what kind of motion, rolling or slipping, will have the drop after unpinning from the surface. Intuitively, rolling is expected to occur when the drop shape is close to circular (contact angle is close to 180°), while slipping can occur even on a hydrophylic surface (the contact angle is smaller than 90°). Such expectations were confirmed in Ref. 41 on the basis of the solution of the Navier-Stokes and Cahn-Hillard equations. The drops considered in the present paper had an equilibrium contact angle of about 150°. One can assume that such a drop will slip along the surface, because it has considerable contact area with the solid (see Fig. 6).

The model considered in the present paper suggests that the sticking force on a drop on the SLIPS can be caused, at least in part, by the hidden roughness. Full microscopic insight to that problem can be obtained by using the density functional theory for binary mixtures which is based on the microscopic considerations of fluid-fluid and fluid-solid interactions. Such a theory, called as Fundamental Measure Theory (FMT), was developed by Rosenfeld.[17] However, the application of the FMT to the above problem is extremely difficult for computational reasons and up to our best knowledge, no attempts have been

done in this directions. The SLIPS were examined theoretically only on the basis of the traditional thermodynamics involving the macroscopic concepts of surface tensions.[5,42,43]

5 Appendix. Free energy contributions and solution of the Euler-Lagrange equation

The total Helmholtz free energy $F[\rho_f(\mathbf{r})]$ of a fluid under the external potential generated by a solid is expressed as the sum of an ideal gas free energy, $F_{id}[\rho_f(\mathbf{r})]$, a free energy $F_{hs}[\rho_f(\mathbf{r})]$ of a reference system of hard spheres, a free energy $F_{attr}[\rho_f(\mathbf{r})]$ due to the attractive interactions between fluid molecules (in the mean field approximation), and a free energy $F_{fs}[\rho_f(\mathbf{r})]$ due to the interactions between fluid and solid. These contributions to the free energy can be represented as follows[28,44]

$$F_{id}[\rho_f(\mathbf{r})] = k_B T \int d\mathbf{r}\rho_f(\mathbf{r})\{\log[\Lambda^3\rho_f(\mathbf{r})] - 1\}, \tag{A. 1}$$

$$F_{hs}[\rho_f(\mathbf{r})] = \int d\mathbf{r}\rho_f(\mathbf{r})\Delta\Psi_{hs}(\mathbf{r}) \tag{A. 2}$$

where $\Lambda = h_P/(2\pi m k_B T)^{1/2}$ is the thermal de Broglie wavelength, h_P and k_B are the Planck and Boltzmann constants, respectively, T is the absolute temperature, m is the mass of a fluid molecule,

$$\Delta\Psi_{hs}(\mathbf{r}) = k_B T \eta_{\bar{\rho}_f} \frac{4 - 3\eta_{\bar{\rho}_f}}{(1 - \eta_{\bar{\rho}_f})^2} , \tag{A. 3}$$

$\eta_{\bar{\rho}_f} = \frac{1}{6}\pi\bar{\rho}_f(\mathbf{r})\sigma_{ff}^3$ is the packing fraction of the fluid molecules, σ_{ff} is the fluid hard core diameter, and $\bar{\rho}(\mathbf{r})$ is the smoothed density defined as

$$\bar{\rho}(\mathbf{r}) = \int d\mathbf{r}'\rho(\mathbf{r}')W(|\mathbf{r}-\mathbf{r}'|)\ . \tag{A. 4}$$

The weighting function $W(|\mathbf{r}-\mathbf{r}'|)$ is selected in the form[45]

$$W(|\mathbf{r}-\mathbf{r}'|) \quad = \quad \begin{cases} \frac{3}{\pi\sigma_{ff}^3}\left(1-\frac{r}{\sigma_{ff}}\right), & r \le \sigma_{ff} \\ 0, & r > \sigma_{ff} \end{cases}$$

where $r = |\mathbf{r}-\mathbf{r}'|$.

The contribution to the excess free energy due to the attraction between the fluid-fluid molecules is calculated in the mean-field approximation

$$F_{attr}[\rho_f(\mathbf{r})] = \frac{1}{2}\int\int d\mathbf{r}d\mathbf{r}'\rho_f(\mathbf{r})\rho_f(\mathbf{r}')\phi_{ff}(|\mathbf{r}-\mathbf{r}'|) \tag{A. 5}$$

where $\phi_{ff}(|\mathbf{r}-\mathbf{r}'|)$ is the Lennard-Jones potential of the fluid-fluid interactions.

The last contribution, $F_{fs}[\rho_f(\mathbf{r})]$, is given by the expression

$$F_{fs}[\rho_f(\mathbf{r})] = \int_V d\mathbf{r}\rho_f(\mathbf{r})\left[U_{fs}(\mathbf{r}) + U_{fl}(\mathbf{r}) + U_e(\mathbf{r})\right] \tag{A. 6}$$

where V is the volume occupied by the fluid, and $U_{fs}(\mathbf{r})$, $U_{fl}(\mathbf{r})$, and $U_e(\mathbf{r})$ are provided by eqn (3), 5, and 6.

The Euler-Lagrange equation for the fluid density distribution $\rho_f(x,h)$ obtained by minimizing the Helmholtz free energy can be represented in the following general form

$$\log[\Lambda^3 \rho_f(x,h)] - Q_f(x,h) = \frac{\lambda}{k_B T} \tag{A. 7}$$

where λ is a Lagrange multiplier and the function $Q_f(x,h)$ is given by

$$Q_f(x,h) = -\frac{1}{k_B T}\left[\Delta\Psi_{hs}(x,h) + \overline{\Delta\Psi'}_{hs}(x,h) + U_{ff}(x,h) + U_{fs}(x,h) + U_e(x)\right] \tag{A. 8}$$

where

$$U_{ff}(x,h) = \int\int dx' dh' \rho_f(x',h') \phi_{ff,y}(|x-x'|,|h-h'|), \tag{A. 9}$$

$$\overline{\Delta\Psi'}_{hs}(x,h) = \int\int dx' dh' \rho_f(x',h') W_y(|x-x'|,|h-h'|)\ \frac{\partial}{\partial\bar{\rho}} \Delta\ \Psi_{hs}(\bar{\rho})|_{\bar{\rho}=\bar{\rho}_f(x',h')}\,, \tag{A. 10}$$

$\phi_{ff,y}(|x-x'|,|h-h'|)$ and $W_y(|x-x'|,|h-h'|)$ are obtained by integrating the potential $\phi_{ff}(|\mathbf{r}-\mathbf{r}'|)$ and the weighted function $W(|\mathbf{r}-\mathbf{r}'|)$ with respect to y from $-\infty$ to $+\infty$.

When calculating $U_{ff}(x,h)$ of the Euler-Lagrange equation arising due to the long-range fluid-fluid interactions, a cutoff at a distance equal to four molecular diameters σ_{ff} for the range of Lennard-Jones attraction was employed.

The general iteration procedure used in this paper is explained in Refs 14,25. Here we will discuss only the selection of the initial guess which constitutes an important part of the calculations. As shown in Ref. 14,25, the location of a stable drop on a nonuniform surface depends on the properties of the surface and the size of the drop. When the initial guess is selected arbitrarily, usually as a "rectangular" drop at an arbitrary location on the surface,[13] the iterations transform its location and shape toward the location and shape of the stable drop. The required number of iterations depends on how close is the initial

guess to the location of the solution of the Euler-Lagrange equation and how quick is the transformation of the intermediate density distribution during iterations. For the case considered in the present paper, the convergence of the iteration procedure is extremely slow and, for this reason, the choice of the initial guess has a critical importance in finding the solution in a reasonable time. For the selection of an initial FDD a special approach was developed which is based on the following observation.

Let us suppose that the iterations start with a rectangular initial guess located arbitrarily on the surface of SSM (see Fig. 12a) and that one keeps track of the difference $\Delta\rho_{f,i}(x,h) = \rho_{f,i+1}(x,h) - \rho_{f,i}(x,h)$ between the density distributions, $\rho_{f,i}(x,h)$ and $\rho_{f,i+1}(x,h)$, provided by two consecutive iterations. Then, after 50 - 100 iterations this difference as function of x and h has, generally, one of the three shapes presented in Fig. 12b, c, and d where the light (dark) areas represent positive (negative) values of $\Delta\rho_{f,i}(x,h)$. Figs. 12b and c indicate the tendency of the density distribution $\rho_{f,i}(x,h)$ to "move" in the direction of the positive part of $\Delta\rho_{f,i}(x,h)$, i.e. to the left for Fig. 12b and to the right for Fig. 12c. Fig. 12d indicates the case in which the initial guess is selected almost at the location of the solution of Euler-Lagrange equation.

On the basis of the above observation, we first selected (see Fig. 13) four initial guesses of the same rectangular shape at the positions of the minimum, maximum, and of the two inflection points of the net potential $U_{net}(\mathbf{r})$ (points A, C, B, and D in Fig. 5).

After several iterations (about 100), the differences $\Delta\rho_{f,i}(x,h)$ for each initial guess were analyzed. The solution is located between the points where the distributions of $\Delta\rho_{f,i}(x,h)$ move towards each other. To determine the location of the solution more

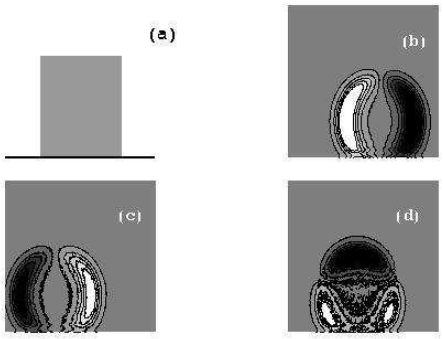

Figure 12: (a) Initial guess for the iteration procedure. (b), (c), and (d) Possible graphs of the differences between two consecutive iterations. Dark areas correspond to negative values of this differences and light areas correspond to positive values.

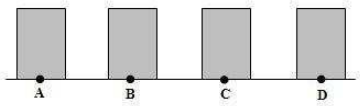

Figure 13: Four starting initial guesses. The meaning of points A, B, C, and D is provided in Fig. 5

precisely, the described procedure was applied to the interval between those specific points found in the previous part of the calculations.

The analysis of $\Delta\rho_{f,i}(x,h)$ provides information whether the obtained solution is stable or unstable. In more details, this issue is discussed in Appendix B of Ref. 46.

To avoid the divergence of the iteration procedure, the input density profile $\rho^{in}_{f,i}(x,h)$ for the $(i+1)$-th iteration $\rho_{f,i+1}(x,h)$, generated by the Euler-Lagrange equation, was selected as follows[28]

$$\rho^{in}_{f,i}(x,h) = (1-\gamma)\rho^{in}_{f,i-1}(x,h) + \gamma\rho_{f,i}(x,h) \qquad \text{(A. 11)}$$

where $\rho_{f,i}(x,h)$ is the i-th iteration and the constant $\gamma = 0.1$. As a measure of the precision of the iterations the dimensionless quantity

$$\delta = \int_V dxdh \left[\rho_{f,i+1}(x,h) - \rho^{in}_{f,i}(x,h)\right]^2 / \left(\int_V dxdh\rho_{f,i}(x,h)\right)^2$$

was introduced. The iterations were carried out on a two dimensional grid with a spacing equal to $0.1\sigma_{ff}$ until δ became smaller than 10^{-7}.

References

[1] R.N.Wenzel, *Ind.Eng.Chem.*, 1936, **28**, 988-994.

[2] A.B.D.Cassie and S.Baxter, *Trans.Faraday Soc.*, 1944, **40**, 0546-0550.

[3] M.A.Sarshar, W. Xu, and C-H. Choi. in Mittal, K.L., ed. Adhesion and Adhesives:Fundamental and Applied Aspects: Advances in Contact Angle, Wettability and Adhesion. 2013, 3-18, Somerset, NJ, USA: John Wiley & Sons.

[4] P.Tarazona and R.Evans, *Mol. Phys.*, 1984, **52**, 847-857.

[5] T.S.Wong, S.H.Kang, S.K.Y.Tang, E.J.Smythe, B.D.Hatton, A.Grinthal and J.Aizenberg, *Nature*, 2011, **477**, 443-447.

[6] W.Ma, Y.Higaki, H.Otsuka and A.Takahara, *Chemical Communications.*, 2013, **49**, 597-599.

[7] A.K.Epstein, T.S.Wong, R.A.Belisle, E.M.Boggs and J.Aizenberg, *Proceedings of the National Academy of Sciences of the United States of America.*, 2012, **109**, 13182-13187.

[8] P.W.Wilson, W.Z.Lu, H.J.Xu, P.Kim, M.J.Kreder, J.Alvarenga and J.Aizenberg, *Physical Chemistry Chemical Physics*, 2013, **15**, 581-585.

[9] J.D.Smith, R.Dhiman, S.Anand, E.Reza-Garduno, R.E.Cohen, G.H.McKinley and K.K.Varanasi, *Soft Matter.*, 2013, **9**, 1772-1780.

[10] R.Qiu, Q.Zhang, P.Wang, L.Jiang, J.Hou, W.Guo and H.Zhang, *Coll. Surf. A*, 2014, **453**, 132-141.

[11] L.Xiao, J.Li, S.Mieszkin, A.Di Fino, A.S.Clare, M.E.Callow, J.A.Callow, M.Grunze, A.Rosenhahn and P.A.Levkin, *ACS Applied Materials & Interfaces*, 2013, **5**, 10074-80.

[12] J.Li, T.Kleintschek, A.Rieder, Y.Cheng, T.Baumbach, U.Obst, T.Schwartz and P.A.Levki. *ACS Applied Materials & Interfaces*, 2013, **5**, 6704-6711.

[13] E.Ruckenstein and G.O.Berim, *Advances in Colloid and Interface Science*, 2010, **157**, 1-33.

[14] G.O.Berim and E.Ruckenstein, *J. Chem. Phys.*, 2008, **129**, 114709.

[15] C.D. Daub, J.H. Wang, S. Kudesia, D. Bratko and A. Luzar, *Faraday Discussions*, 2010, **146**, 67-77.

[16] R.Evans and P.Tarazona, *Phys. Rev. A*, 1983, **28**, 1864-1868.

[17] Y.Rosenfeld, *Phys. Rev. Lett.*, 1989, **63**, 980-983.

[18] G.O.Berim and E.Ruckenstein, *J. Chem. Phys.*, 2008, **128**, 134713.

[19] F.Ancilotto and F.Toigo, *J. Chem. Phys.*, 2000, **112**, 4768-4772.

[20] S. Nordholm, M. Johnson and B. C. Freasier, *Aust. J. Phys.*, **33**, 2139 (1980).

[21] A.González, J.A.White, F.L.Román and S.Velasco, *Phys. Rev. Lett.*, 1997, **79**, 2466-2469.

[22] A.González, J.A.White, F.L.Román and R.Evans, *J. Chem. Phys.*, 1998, **109**, 3637-3650.

[23] J.A.White and S.Velasco *Phys. Rev. E*, 2000, **62**, 4427-4430.

[24] J.A.White, A.González,F.L.Román and S.Velasco, *Phys. Rev. Lett.*, 2000, **84**, 1220-1223.

[25] G.O.Berim and E.Ruckenstein, *J.Chem. Phys.*, 2008, **129**, 014708.

[26] M.J. de Ruijter, T.D.Blake and J. De Coninck, *Langmuir*, 1999, **15**, 7836-7847.

[27] N.Giovambattista, P.G.Debenedetti and P.J.Rossky, *J. Phys. Chem. B*, 2007, **111**, 9581-9587.

[28] P.Tarazona, *Physical Review A*, 1985, **31**, 2672-2679.

[29] F.Porcheron, P.A.Monson and M.Schoen, *Phys.Rev. E*, 2006, **73**, 041603.

[30] A.P. Malanoski, B.J. Johnson and J.S. Erickson, *Nanoscale*, 2014, **6**, 5260-5269.

[31] G. Scocchi, D. Sergi, C. DAngelo, and A. Ortona, *Phys.Rev E*, 2011, **84**, 061602.

[32] B.A.Pethica, *Rep. Prog. Appl. Chem.*, 1961, **46**, 14; B.A.Pethica, *J. Colloid Interface Sci.*, 1977, **62**, 567-569.

[33] R. David and A.W. Neumann, *Langmuir*, 2007, **23**, 11999-12002.

[34] L. Schimmele and S. Dietrich, *Eur.Phys.J. E*,2009, **30**, 427430.

[35] L.Gao and T.McCarthy, *Langmuir*, 2007, **23**, 3762-3765.

[36] McHale, G. Langmuir, 2007, 23, 8200-8205.

[37] M.Nosonovsky, *Langmuir*, 2007, **23**, 99199920.

[38] C.G.L.Furmige, J.Colloid.Sci., 1962, **17**, 309.

[39] M.Callies and D.Quéré, *Soft Matter*, 2005, **1**, 55.

[40] M. Nosonovsky and B. Bhushan (Eds), *Green Tribology: Biomimetics, Energy Conservation and Sustainability*, Ch. 2, Springer, 2012.

[41] S.P.Thampi, R.Adhikari and R.Govidarajan, *Langmuir*, 2013, **29**, 3339-3346.

[42] V.Hejazi and M.Nosonovsky, *Langmuir*, 2012, **28**, 2173-2180.

[43] V.Hejazi and M.Nosonovsky, *Colloid and Polymer Science*, 2013, **291**, 329-338.

[44] P.Tarazona, U.M.B.Marconi and R.Evans, *Mol. Phys.*, 1987, **60**, 573-595.

[45] R.N.Nilson and S.K.Griffiths, *J. Chem. Phys.*, 1999, **111**, 4281-4290.

[46] G.O.Berim and E.Ruckenstein, *Nanoscale*, 2015, **7**, 3088-3099.